Dalton Transactions

ROYAL SOCIETY OF CHEMISTRY

COMMUNICATION

View Article Online
View Journal | View Issue

Cite this: *Dalton Trans.*, 2025, **54**, 15696

Received 4th August 2025,
Accepted 6th September 2025

DOI: 10.1039/d5dt01863c

rsc.li/dalton

Pressure-induced tuning of the triangular-honeycomb structure of ferroelectric quantum spin liquid candidate, $TbInO_3$

Christopher J. Ridley, [a] Aly H. Abdeldaim,[b,c,d] Craig L. Bull, [c,e] Katherine Tustain[f,g] and Lucy Clark *[b]

The pressure response of the triangular-honeycomb-structured quantum spin liquid candidate, $TbInO_3$, has been determined *via* neutron powder diffraction up to 5.75(5) GPa. The system retains hexagonal symmetry up to the maximum pressure considered. The structure was found to compress less anisotropically than related compounds, though it is more compressible within the 2D plane than between subsequent layers. Through extracting the O-atom coordinates we find experimental evidence that may suggest the enhancement of ferroelectricity at pressures as low as 3 GPa.

Geometrically frustrated magnetic systems often exhibit non-trivial and highly degenerate ground states, which remain a subject of active research.[1,2] In such systems, quantum and thermal fluctuations can suppress long-range magnetic order, resulting in exotic ground states such as quantum spin liquids.[3,4] Such systems are highly susceptible to external perturbations, such as pressure, which can be used to continuously tune exchange parameters.[5,6] The rare-earth magnet $TbInO_3$ has generated significant interest as a highly-frustrated quantum spin liquid candidate.[7,8] Previous muon spin relaxation, neutron diffraction and magnetic susceptibility measurements show the absence of any long-range ordering in the material down to 460 mK, despite an antiferromagnetic Weiss constant, θ_{CW} = −17.19(3) K.[7] Specific heat measurements find no evidence of a phase transition down to 150 mK.[9]

At ambient conditions, $TbInO_3$ is isostructural with the hexagonal rare-earth (R) manganates, $RMnO_3$, formed of layers of non-magnetic corner-shared $[InO_5]^{7-}$ trigonal–bipyramidal units separated by a hexagonal magnetic sub-lattice formed of 7-fold coordinated Tb^{3+} ions. The $[InO_5]^{7-}$ polyhedra are clustered into trimers, tilting around a shared bridging oxygen. There are two distinct Tb^{3+} sites, Tb1 sitting at the hexagonal centre points ($P6_3cm$, Wyckoff 2*a*), and Tb2 forming the honeycomb structure (Wyckoff 4*b*). This forms a slightly distorted two-dimensional triangular lattice of $S_{eff} = \frac{1}{2}$ moments, with two distinct Tb nearest-neighbour interactions. This model has been confirmed as an adequate description of the structure over the temperature range 0.46–400 K using high-resolution neutron powder-diffraction, revealing only a gradual expansion of lattice constants upon heating.[7] Crystal-field modelling to inelastic neutron scattering data suggests that below $T \sim 7.5$ K, the two Tb sites are magnetically distinct, and the Tb^{3+} sub-lattice is expected to dilute to an undistorted honeycomb network of the Wyckoff 4*b* sites only.[7] The lack of long-range magnetic order on the honeycomb-lattice points to frustrated anisotropic exchange interactions. This is similarly the case in the Kitaev spin liquid candidates, some of which are known to be highly tunable with pressure,[10] or can only be stabilised using high-pressure synthesis.[11] For example, pressure is known to affect the anisotropic exchange interactions in α-$RuCl_3$, inducing exotic magnetic phase behaviour.[12]

In addition to this exotic magnetic behaviour, the structural trimerisation of $TbInO_3$ breaks inversion symmetry, inducing an out-of-plane distortion between the two distinct Tb-sites. This leads to a population imbalance—there are twice as many Tb2 atoms in the unit cell as there are Tb1—resulting in a net ferroelectric polarisation along the *c*-axis.[9,13–17] As the polarisation is a secondary effect in the stabilisation of this phase, $TbInO_3$ is an *improper* ferroelectric; the polarisation is not the primary order-parameter.[14,18] High pressure also brings many benefits to the study of ferroelectric and multiferroic materials.[19] Tan *et al.*[20] considered the effects of hydrostatic pressure on the $RMnO_3$ family from first principles. They concluded that high pressure emulates the effect of varying the R-atom from Pr to Lu, with both resulting in an enhancement

[a]*Neutron Scattering Division, Oak Ridge National Laboratory, Oak Ridge, TN, USA*
[b]*School of Chemistry, University of Birmingham, Edgbaston, Birmingham, B15 2TT, UK. E-mail: l.m.clark@bham.ac.uk*
[c]*ISIS Neutron and Muon Source, Rutherford Appleton Laboratories, Didcot, OX12 9DX, UK*
[d]*Diamond Light Source, Rutherford Appleton Laboratories, Didcot, OX11 0DE, UK*
[e]*School of Chemistry, University of Edinburgh, David Brewster Road, Edinburgh, EH9 3FJ, UK*
[f]*Department of Chemistry and Materials Innovation Factory, University of Liverpool, 51 Oxford Street, Liverpool L7 3NY, UK*
[g]*Royal Society of Chemistry, Thomas Graham House, 290 Cambridge Science Park Milton Rd, Milton, Cambridge CB4 0WF, UK*

of the electric polarisation. The study also highlights the importance of the trimerisation in this enhancement. A number of experimental studies attest to manganates being sensitive to hydrostatic pressures[21–24] with some transforming to an orthorhombic structure at high pressures.[25–29] Gao *et al.*[27] found that, within error, the amplitude of electric polarisation remains constant up to 10 GPa in the case of $LuMnO_3$.

Despite the wealth of work investigating the manganates, there is comparatively little experimental work investigating the effect of high pressure on the related $RInO_3$ compounds. Lin *et al.*[6] used X-ray diffraction and Raman spectroscopy to show that for R = Eu, Gd, Dy, the hexagonal structure compresses anisotropically, though remains stable up to approximately 17 GPa. Conversely, Dwivedi *et al.*[30] performed a similar study for R = Y, and found a transition to a new orthorhombic phase between 12–15 GPa, with evidence for phase coexistence up to 29 GPa. Indeed, high-pressure structural studies of this family of compounds are non-trivial; X-ray diffraction yields little information on the positions of the lighter O-atoms in the structure, while neutron diffraction can be hampered by the higher absorption of In. However, given the unique combination of ferroelectric and quantum spin liquid behaviour in $TbInO_3$, the application of pressure may provide an appealing route to tune and understand the origin of its exotic structure–property behaviour. Thus, in this present study, we use high-pressure neutron diffraction to probe the structural pressure response of $TbInO_3$.

A polycrystalline sample of $TbInO_3$ was prepared *via* a high-temperature ceramic method. Stoichiometric amounts of Tb_2O_3 and In_2O_3 were ground and intimately mixed, pressed into a pellet and sealed into a platinum tube. The sample was gradually heated in a furnace with four dwell segments: 1473 K for 10 h, 1573 K for 15 h, 1623 K for 5 h and 1673 K for 200 h, followed by furnace cooling. A bright yellow polycrystalline sample was recovered. All measurements reported herein were performed on a sample of $TbInO_3$ taken from the same 10 g batch as reported by Clark *et al.*[7] High-pressure neutron diffraction data were collected for this sample on the PEARL diffractometer at the ISIS Neutron and Muon Source,[31] using a V4 Paris–Edinburgh press with Zirconia Toughened Alumina anvils. The sample was encapsulated using a TiZr gasket, using deuterated methanol : ethanol (4 : 1 by volume) as a pressure-transmitting medium, and a small pellet of Pb as a pressure marker. The diffraction data were corrected for anvil attenuation, and models refined using TOPAS v6,[32] see Fig. 1. The sample absorption was accounted for in the refinements using a Lobanov model.[33] The absorption coefficient was freely refined, found to be constant over the measurement series, and subsequently fixed at the average value.

The sample was compressed in steps of ~0.3 GPa up to a maximum pressure of 5.75(5) GPa, remaining in the ambient hexagonal phase throughout. The unit-cell volume of the structure was fitted to a third-order Rydberg–Vinet equation of state,[34] yielding a B_0 = 151(3) GPa, B' = 7(1) and V_0 = 425.71(5) Å, see Fig. 2(a). The unit-cell was found to compress anisotropically, being most compressible along the *a*-axis, with linear compression coefficients of $K_a = -2.09(13)\ \mathrm{TPa}^{-1}$, $K_c = -1.69(16)\ \mathrm{TPa}^{-1}$, see Fig. 2(a). This preferred compressibility is likely due to bond-orientation in the cell. Several Tb–O and In–O are symmetrically constrained to lie parallel to the *c*-axis, while along the *a*-axis the bonds are tilted, and can accommodate additional compression through tilting or distortion of the polyhedra. The preferred compressibility of the *a*-axis is con-

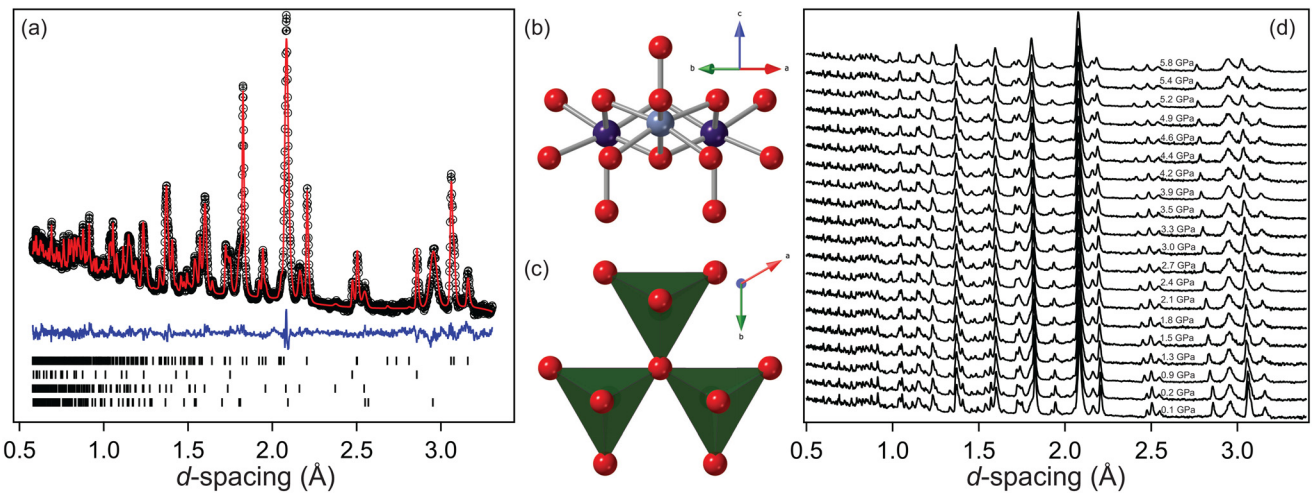

Fig. 1 (a) Rietveld fit to polycrystalline $TbInO_3$ as loaded in the Paris–Edinburgh press at 0.1 GPa. The black markers are the measured data, the red line is the calculated profile, the blue line is the residual to the fit. The tick marks are the expected peak positions from the sample, Pb, Al_2O_3 and ZrO_2 (from top to bottom). (b) Tb-atom structural motif (viewed along the [110]) showing the 7-fold coordination of each Tb-atom, the two distinct Tb sites, and the resultant population imbalance resulting in a net dipole-moment. (c) Trimers formed of $[InO_5]^{7-}$ units as viewed along [001] with the bridging O ion at the centre. The *c*-axis displacement of this bridging O^{2-} ion breaks the inversion symmetry. The full crystal structure is formed of alternating layers of (b) and (c) along the *c*-axis of the unit-cell. (d) Stack plot showing the high-pressure evolution of the neutron diffraction pattern. The uncertainties on the reported pressures is ±0.05 GPa.

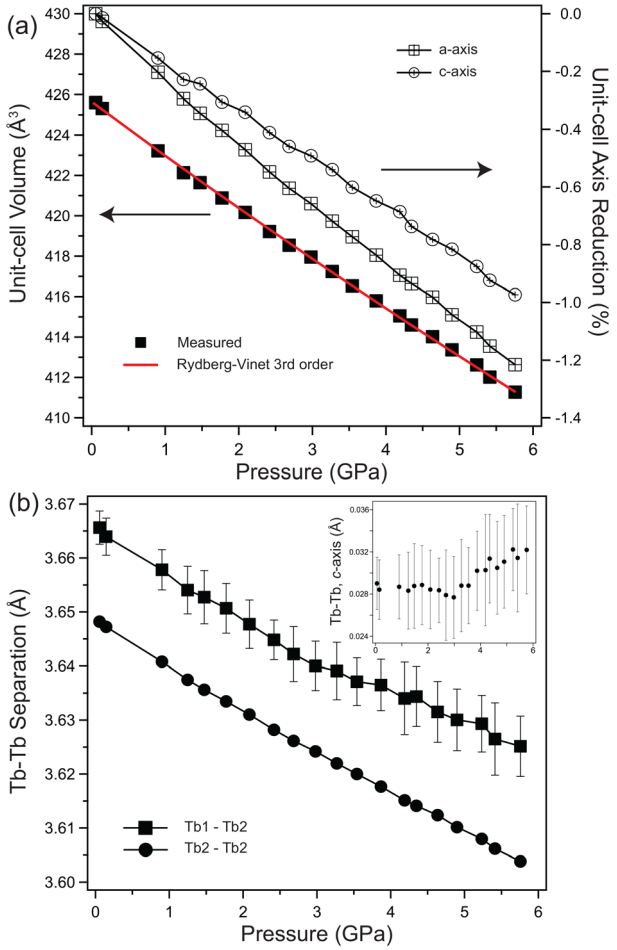

Fig. 2 (a) Determined unit-cell volume and relative unit-cell axis length reductions for $TbInO_3$ as a function of pressure. The unit-cell volume was fitted to a 3rd-order Rydberg–Vinet equation of state as discussed in the main text. (b) The Tb–Tb separation distances as determined from Rietveld refinement to neutron powder diffraction data. The Tb2–Tb2 separation is tightly constrained by the unit-cell axes, error bars are smaller than the marker used. (b, inset) Tb–Tb separation along the *c*-axis, showing a small increase above 3 GPa, but still within error of the ambient pressure value.

sistent with that reported for the related R = Eu, Gd, Dy compounds,[6] however for all three of these compounds a significant reduction of the compressibility was observed with pressure, requiring large first-derivative terms, $B' > 10$, and in the case of $GdInO_3$, there is a clear deviation from the expected behaviour. Similar anisotropic behaviour was reported for some of the manganates,[27] with lower bulk moduli, but comparably large values for B'. Surprisingly for $TbInO_3$, the pressure-hardening is significantly less pronounced than the R = Eu, Gd, Dy analogues. This could be related to the differences in pressure medium used, or may reflect a more isotropic bonding environment or reduced sensitivity of the $[InO_5]^{7-}$ polyhedra to external strain, potentially due to their compact trimerised arrangement. Additional measurements on the R = Eu, Gd, Dy analogues under identical loading conditions would confirm this hypothesis.

Extracting the changes in the Tb unit-cell coordinates, both Tb1–Tb2 and Tb2–Tb2 separations are observed to reduce, see Fig. 2(b). The separation of Tb1 and Tb2 along the *c*-axis shows a tendency to increase with applied pressure above 3 GPa, though unchanging within the error of the measurement, see Fig. 2(b, inset). Both of these observed trends are important, as they may be concomitant with a strengthening of the magnetic exchange interactions between Tb^{3+} moments within the plane and an enhancement of the two-dimensionality of the magnetic exchange. Both of these could be critical to the quantum spin liquid phase proposed to emerge below $T \sim 7.5$ K.

An increase in the separation of the Tb-atoms along the *c*-direction could also be indicative of an enhanced net electric-dipole moment with pressure, consistent with the previous computational predictions.[20] There are four distinct In–O bonds, and six distinct Tb–O bonds in the system. O3 and O4 are equatorial to the In-atoms and serve as the bridge within the trimerised $[InO_5]^{7-}$ arrangement. These atoms also form the longest bond with the Tb atoms. The coordinated tilting of each $[InO_5]^{7-}$ unit results in an alternating 'up'/'down' arrangement between O3/4 in the In-layers. O1 and O2 are apical, and In–O1 is the shortest of the four In-bonds. Similarly Tb1–O1/Tb2–O1 are the shorter of the six Tb–O bonds. With pressure the bridging oxygen bond-lengths change negligibly, while the In–O1 bond is found to reduce most significantly, and more clearly so above 3 GPa, see Fig. 3(a). The refinements showed a degree of correlation between the Tb and O *z*-coordinates, though these observations were found to be robust against a number of alternate starting conditions. As the In-atom is tightly constrained, this result is consistent with the observation in shift of the Tb-atom, and reflects the tensioning between the rigidity of the $[InO_5]^{7-}$ arrangement against the formation of an enhanced dipole moment in the Tb-layers. The longest Tb–O bonds are Tb1–O3 and Tb2–O4, the largest contributor to the net dipole moment in the cell; Tb1–O3 remains unchanged with pressure, while Tb1–O4 reduces, see Fig. 3(b). At first, this is suggestive of a reduction in the net dipole moment, though there is a larger total net separation of positive (Tb^{3+}) and negative (O^{2-}) charge centres, thus likely enhancing the net electric polarization along *c*, see Fig. 3(c). This argument assumes that a 'point-charge' model is accurate for this material. While this has been calculated for $YMnO_3$ to be a close to valid assumption at ambient pressure,[35] pressure induced changes in covalency could result in changes to the Born effective charge, and as such direct measurements are required to validate this finding unequivocally.

To summarise, we have found that $TbInO_3$ remains stable in the $P6_3cm$ hexagonal phase up to 5.75(5) GPa, the highest pressure considered in this study. The neutron absorption of In brings with it challenges from a neutron diffraction perspective, but nevertheless, a robust Rietveld analysis has allowed us to extract meaningful atomic coordinates, including of the O-atoms. From this analysis, we can speculate that there will be an enhanced electric dipole moment in $TbInO_3$ at pressures as low as 3 GPa, as well as the tuning of the struc-

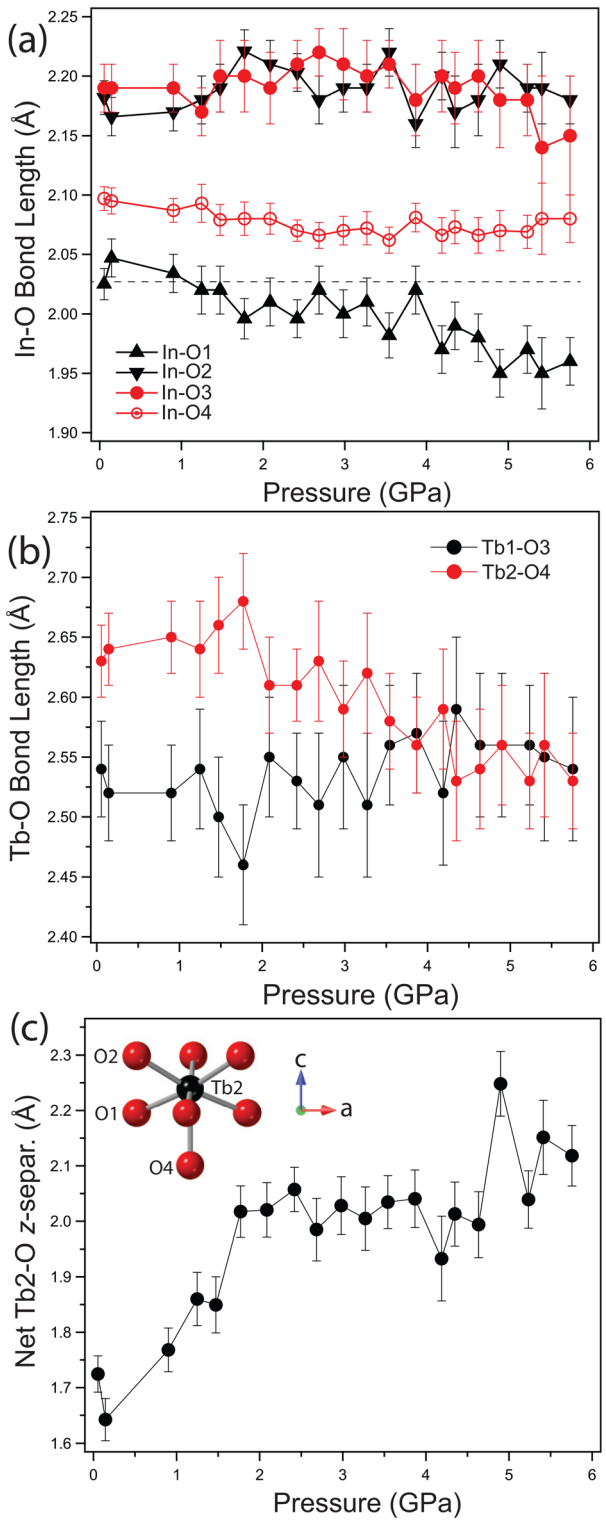

Fig. 3 (a) Four distinct In–O bond lengths for $TbInO_3$ as a function of pressure. O1 and O2 are apical, O3 and O4 are equatorial to the In atom along the *c*-axis. (b) Long Tb–O bond lengths, showing that Tb1–O3 remains constant, while Tb2–O4 contracts. (c) Net separation of $(Tb2)^{3+}$ O^{2-} along the *c*-axis showing that despite a reduction in Tb2–O4 a net dipole moment increase is possible.

tural parameters that govern the two-dimensional magnetic exchange interactions of the proposed quantum spin liquid ground state, which should be tested by direct measurement of the dipole moment and exchange interactions under pressure. Indeed, given that the nature of the quantum spin liquid phase emerging in $TbInO_3$ and how it interacts with the co-existing ferroelectricity remain unknown, this work provides a critical foundation and motivation for future high-pressure and low-temperature studies. All of this work was performed at room temperature, but it would be very interesting to compare these with the pressure response below $T \sim 7.5$ K. Though technically challenging, such future experiments would likely provide a rewarding understanding of the wider magnetic phase diagram of $TbInO_3$ that controls its unique structure–property behaviour.

Conflicts of interest

There are no conflicts to declare.

Data availability

Raw neutron powder diffraction data are available open access *via* the link provided in ref. 36. Refined models are available as crystallographic information files *via* the Inorganic Crystal Structure Database (ICSD).

CCDC 2474418–2474437 contain the supplementary crystallographic data for this paper.[37a–t]

Acknowledgements

The authors thank the ISIS Neutron and Muon Source for providing access to the PEARL diffractometer,[36] and the Science and Technology Facilities Council for supporting this work, including a PhD studentship to AHA under the ISIS Facility Development and Utilisation Studentship scheme. A portion of this research was supported by resources at the Spallation Neutron Source, a DOE Office of Science User Facility operated by the Oak Ridge National Laboratory. The authors acknowledge Phoenix Pleasant (Oak Ridge National Laboratory) for preparing the article TOC artwork.

References

1 J. E. Greedan, *J. Mater. Chem.*, 2001, **11**, 37–53.
2 R. Moessner and A. P. Ramirez, *Phys. Today*, 2006, **59**, 24–29.
3 P. W. Anderson, *Mater. Res. Bull.*, 1973, **8**, 153–160.
4 L. Balents, *Nature*, 2010, **464**, 199–208.
5 S. A. Zvyagin, D. Graf, T. Sakurai, S. Kimura, H. Nojiri, J. Wosnitza, H. Ohta, T. Ono and H. Tanaka, *Nat. Commun.*, 2019, **10**, 1064.

6 C. Lin, J. Liu, Y. Li, X. Li and R. Li, *Solid State Commun.*, 2013, **173**, 51–55.
7 L. Clark, G. Sala, D. D. Maharaj, M. B. Stone, K. S. Knight, M. T. Telling, X. Wang, X. Xu, J. Kim, Y. Li, *et al.*, *Nat. Phys.*, 2019, **15**, 262–268.
8 T. S. Jung, X. Xu, J. Kim, B. H. Kim, H. J. Shin, Y. J. Choi, E.-G. Moon, S.-W. Cheong and J. H. Kim, *Nat. Phys.*, 2023, **19**, 1611–1616.
9 J. Kim, X. Wang, F.-T. Huang, Y. Wang, X. Fang, X. Luo, Y. Li, M. Wu, S. Mori, D. Kwok, E. D. Mun, V. S. Zapf and S.-W. Cheong, *Phys. Rev. X*, 2019, **9**, 031005.
10 G. Bastien, G. Garbarino, R. Yadav, F. J. Martínez-Casado, R. Beltrán Rodríguez, Q. Stahl, M. Kusch, S. P. Limandri, R. Ray, P. Lampen-Kelley, *et al.*, *Phys. Rev. B*, 2018, **97**, 241108.
11 T. Weinhold, C. Wang, F. Seewald, V. Grinenko, Y. Imai, F. Sato, K. Ohgushi, H.-H. Klauss and R. Sarkar, *Phys. Rev. B*, 2024, **109**, 014440.
12 Q. Stahl, T. Ritschel, G. Garbarino, F. Cova, A. Isaeva, T. Doert and J. Geck, *Nat. Commun.*, 2024, **15**, 8142.
13 S. C. Abrahams, *Struct. Sci.*, 2001, **57**, 485–490.
14 Y. Kumagai and N. A. Spaldin, *Nat. Commun.*, 2013, **4**, 1540.
15 H. Sim, J. Oh, J. Jeong, M. D. Le and J.-G. Park, *Struct. Sci.*, 2016, **72**, 3–19.
16 B. Paul, S. Chatterjee, S. Gop, A. Roy, V. Grover, R. Shukla and A. K. Tyagi, *Mater. Res. Express*, 2016, **3**, 075703.
17 C. Min, Y. Wu, Y. Li, C. Zhou, S.-W. Cheong, X. Lu, T. Zhou and L. Zhang, *Crystals*, 2023, **13**, 287.
18 A. H. Mokhtar, D. Serban, D. G. Porter, F. Lichtenberg, S. P. Collins, A. Bombardi, N. A. Spaldin and M. C. Newton, *Nat. Commun.*, 2024, **15**, 3587.
19 E. Gilioli and L. Ehm, *IUCrJ*, 2014, **1**, 590–603.
20 H. Tan, C. Xu, M. Li, S. Wang, B.-L. Gu and W. Duan, *J. Phys.: Condens. Matter*, 2016, **28**, 126002.
21 D. Kozlenko, S. Kichanov, S. Lee, J. G. Park, V. P. Glazkov and B. Savenko, *J. Exp. Theor. Phys. Lett.*, 2005, **82**, 193–197.
22 M. Janoschek, B. Roessli, L. Keller, S. Gvasaliya, K. Conder and E. Pomjakushina, *J. Phys.: Condens. Matter*, 2005, **17**, L425.
23 D. P. Kozlenko, S. E. Kichanov, S. Lee, J. G. Park, V. P. Glazkov and B. N. Savenko, *J. Exp. Theor. Phys. Lett.*, 2006, **83**, 346–350.
24 D. P. Kozlenko, S. E. Kichanov, S. Lee, J. G. Park, V. P. Glazkov and B. N. Savenko, *Crystallogr. Rep.*, 2007, **52**, 407–411.
25 S. M. Feng, L. J. Wang, J. L. Zhu, F. Y. Li, R. C. Yu, C. Q. Jin, X. H. Wang and L. T. Li, *J. Appl. Phys.*, 2008, **103**, 026102.
26 L. J. Wang, S. M. Feng, J. L. Zhu, Q. Q. Liu, Y. C. Li, X. D. Li, J. Liu and C. Q. Jin, *High Press. Res.*, 2010, **30**, 258–264.
27 P. Gao, Z. Chen, T. A. Tyson, T. Wu, K. H. Ahn, Z. Liu, R. Tappero, S. B. Kim and S.-W. Cheong, *Phys. Rev. B: Condens. Matter Mater. Phys.*, 2011, **83**, 224113.
28 C. Lin, J. Liu, X. Li, Y. Li, S. Chu, L. Xiong and R. Li, *J. Appl. Phys.*, 2012, **112**, 113512.
29 M. Ottesen, E. Ehrenreich-Petersen, C. H. Kronbo, F. Baudelet, L. Nataf, I. Kantor, M. R. V. Jørgensen and M. Bremholm, *Phys. Rev. B*, 2023, **107**, 134115.
30 A. Dwivedi, H. K. Poswal, R. Shukla, S. Velaga, B. D. Sahoo, V. Grover and M. N. Deo, *High Press. Res.*, 2019, **39**, 17–35.
31 C. L. Bull, N. P. Funnell, M. G. Tucker, S. Hull, D. J. Francis and W. G. Marshall, *High Press. Res.*, 2016, **36**, 493–511.
32 A. A. Coelho, *Appl. Crystallogr.*, 2018, **51**, 210–218.
33 N. N. Lobanov and L. Alte da Veiga, 6th European Powder Diffraction Conference, Budapest, Hungary, 1998.
34 P. Vinet, J. H. Rose, J. Ferrante and J. R. Smith, *J. Phys.: Condens. Matter*, 1989, **1**, 1941.
35 B. B. Van Aken, T. T. M. Palstra, A. Filippetti and N. A. Spaldin, *Nat. Mater.*, 2004, **3**, 164–170.
36 L. Clark, C. L. Bull, C. J. Ridley, K. Tustain and A. Abdeldaim, in *STFC ISIS Neutron and Muon Source*, 2018. DOI: **10.5286/ISIS.E.RB1900039**.
37 (*a*) CCDC 2474418: Experimental Crystal Structure Determination, 2025, DOI: **10.5517/ccdc.csd.cc2p1tyj**; (*b*) CCDC 2474419: Experimental Crystal Structure Determination, 2025, DOI: **10.5517/ccdc.csd.cc2p1tzk**; (*c*) CCDC 2474420: Experimental Crystal Structure Determination, 2025, DOI: **10.5517/ccdc.csd.cc2p1v0m**; (*d*) CCDC 2474421: Experimental Crystal Structure Determination, 2025, DOI: **10.5517/ccdc.csd.cc2p1v1n**; (*e*) CCDC 2474422: Experimental Crystal Structure Determination, 2025, DOI: **10.5517/ccdc.csd.cc2p1v2p**; (*f*) CCDC 2474423: Experimental Crystal Structure Determination, 2025, DOI: **10.5517/ccdc.csd.cc2p1v3q**; (*g*) CCDC 2474424: Experimental Crystal Structure Determination, 2025, DOI: **10.5517/ccdc.csd.cc2p1v4r**; (*h*) CCDC 2474425: Experimental Crystal Structure Determination, 2025, DOI: **10.5517/ccdc.csd.cc2p1v5s**; (*i*) CCDC 2474426: Experimental Crystal Structure Determination, 2025, DOI: **10.5517/ccdc.csd.cc2p1v6t**; (*j*) CCDC 2474427: Experimental Crystal Structure Determination, 2025, DOI: **10.5517/ccdc.csd.cc2p1v7v**; (*k*) CCDC 2474428: Experimental Crystal Structure Determination, 2025, DOI: **10.5517/ccdc.csd.cc2p1v8w**; (*l*) CCDC 2474429: Experimental Crystal Structure Determination, 2025, DOI: **10.5517/ccdc.csd.cc2p1v9x**; (*m*) CCDC 2474430: Experimental Crystal Structure Determination, 2025, DOI: **10.5517/ccdc.csd.cc2p1vby**; (*n*) CCDC 2474431: Experimental Crystal Structure Determination, 2025, DOI: **10.5517/ccdc.csd.cc2p1vcz**; (*o*) CCDC 2474432: Experimental Crystal Structure Determination, 2025, DOI: **10.5517/ccdc.csd.cc2p1vd0**; (*p*) CCDC 2474433: Experimental Crystal Structure Determination, 2025, DOI: **10.5517/ccdc.csd.cc2p1vf1**; (*q*) CCDC 2474434: Experimental Crystal Structure Determination, 2025, DOI: **10.5517/ccdc.csd.cc2p1vg2**; (*r*) CCDC 2474435: Experimental Crystal Structure Determination, 2025, DOI: **10.5517/ccdc.csd.cc2p1vh3**; (*s*) CCDC 2474436: Experimental Crystal Structure Determination, 2025, DOI: **10.5517/ccdc.csd.cc2p1vj4**; (*t*) CCDC 2474437: Experimental Crystal Structure Determination, 2025, DOI: **10.5517/ccdc.csd.cc2p1vk5**.